

# DRAFT

# CMS Paper

*The content of this note is intended for CMS internal use and distribution only*

2023/11/20

Archive Hash: 32611a6

Archive Date: 2023/09/28

## Search for Dark Matter Produced in Association with a Resonant Bottom-Quark Pair in Proton-Proton Collisions at $\sqrt{s} = 13 \text{ TeV}$

The CMS Collaboration

### Abstract

A search for dark matter (DM) produced in association with a resonant  $b\bar{b}$  pair is performed in proton-proton collisions at a center-of-mass energy of 13 TeV collected with the CMS detector during the Run 2 of the Large Hadron Collider. The analyzed data sample corresponds to an integrated luminosity of  $137 \text{ fb}^{-1}$ . Results are interpreted in terms of a novel theoretical model of DM production at the LHC that predicts the presence of a Higgs-boson-like particle in the dark sector, motivated simultaneously by the need to generate the masses of the particles in the dark sector and the possibility to relax constraints from the DM relic abundance by opening up a new annihilation channel. If such a dark Higgs boson decays into standard model (SM) states via a small mixing with the SM Higgs boson, one obtains characteristic large-radius jets in association with missing transverse momentum that can be used to efficiently discriminate signal from backgrounds. Limits on the signal strength of different dark Higgs boson mass hypotheses below 160 GeV are set for the first time with CMS data.

This box is only visible in draft mode. Please make sure the values below make sense.

PDFAuthor:	M. Cremonesi, A. Das, M. Donega, S. Eisenberger, E. Ertorer, A. Hall, M. Hildreth, B. Jayatilaka, J. Lee, N. Macilla, M. Marchegiani, C.-S. Moon, I. Pedraza, N. Smith, T. Tomei, D. Valsecchi, R. Wallny, M. Wassmer1, Z. Ye
PDFTitle:	Search for Dark Matter Produced in Association with a Resonant Bottom-Quark Pair
PDFSubject:	CMS
PDFKeywords:	CMS, physics, software, computing

Please also verify that the abstract does not use any user defined symbols



1 It is well established from astrophysical observations that most of the matter in the Universe is  
2 comprised of dark matter (DM) [1]. However, its particle nature remains unknown and cannot  
3 be accommodated within the standard model (SM). One of the leading hypotheses is that DM is  
4 composed of stable, electrically neutral, massive particles which interact with baryons at least  
5 via the gravitational force. If such a DM particle also interacts non-gravitationally with SM  
6 particles, then DM could be produced in proton-proton collisions at the Large Hadron Collider  
7 (LHC) at CERN.

8 Since DM particles, once produced, do not leave any detectable signal in the detector, they  
9 cannot be directly observed. However, their presence can be inferred if they are produced in  
10 association with a visible SM particle X. Such processes generate final states commonly referred  
11 to as mono-X or  $p_T^{\text{miss}} + X$  signatures, where  $p_T^{\text{miss}}$  is the missing transverse momentum [2].  
12 Typically, the most sensitive analysis channel to DM production is the one that searches for  
13 DM produced in association with a gluon or a quark emitted as initial state radiation (ISR),  
14 known as the mono-jet channel.

15 The mono-jet DM searches at the LHC [3, 4] have strongly constrained the parameter space  
16 in which DM particles can obtain their relic abundance from direct annihilation into SM final  
17 states. This tension is relaxed if DM particles are not the lightest state in the dark sector, lead-  
18 ing to new annihilation channels. If the DM mass is generated via a Higgs mechanism in the  
19 dark sector and the resulting dark Higgs boson is lighter than DM, a new annihilation channel  
20 where DM particles annihilate into a pair of dark Higgs bosons ( $h_s$ ), with subsequent decay  
21 into SM states, would be possible. This would easily set the observed relic abundance. Assum-  
22 ing a small mixing with the SM Higgs boson, a light dark Higgs boson decays with the same  
23 branching fraction of the SM Higgs boson, which vary depending on its mass. If the dark sector  
24 includes an additional spin-1  $Z'$  mediator, then the probability of the  $Z'$  boson being produced  
25 and radiating a dark Higgs boson (dark-Higgsstrahlung) can be large [5]. A representative  
26 Feynman diagram for this signal model is shown in Fig. 1.

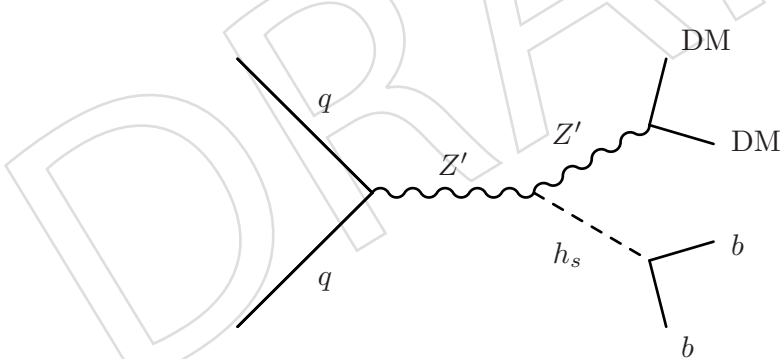


Figure 1: Feynman diagram for the production of a dark Higgs boson in association with DM particles.

27 Searches for dark Higgs boson production in association with DM particles have already been  
28 performed by the ATLAS [6] and the CMS [7] Collaborations. These searches focus on heavier  
29 dark Higgs boson mass hypotheses, larger than 160 GeV. For dark Higgs bosons of such mass  
30 the decay into a pair of W boson is the dominant one. In this paper, we present the search for  
31 the associated production of DM and a light dark Higgs boson (with mass less than 160 GeV),  
32 which decays predominantly into a pair of b quarks, performed for the first time at the LHC.  
33 This final state results in a distinctive signature of large missing transverse momentum, arising  
34 from the decay of the  $Z'$  mediator into DM, and a highly-boosted large-radius jet, originated  
35 by the hadronization of two b quarks from the dark Higgs boson decay. Results are presented

36 for the full dataset of  $137.2 \text{ fb}^{-1}$  collected by the CMS experiment at a center-of-mass energy of  
 37 13 TeV during Run 2 of the LHC.

## 38 1 The CMS detector and event reconstruction

39 The central feature of the CMS apparatus is a superconducting solenoid of 6 m internal diameter,  
 40 providing a magnetic field of 3.8 T. Within the solenoid volume are a silicon pixel and strip  
 41 tracker, a lead tungstate crystal electromagnetic calorimeter (ECAL), and a brass and scintilla-  
 42 tor hadron calorimeter (HCAL), each composed of a barrel and two endcap sections. Forward  
 43 calorimeters extend the pseudorapidity ( $\eta$ ) coverage provided by the barrel and endcap detec-  
 44 tors. Muons are detected in gas-ionization detectors embedded in the steel flux-return yoke  
 45 outside the solenoid.

46 The silicon tracker measures charged particles within the pseudorapidity range  $|\eta| < 2.5$ . Dur-  
 47 ing the LHC running period when the data used in this paper were recorded, the silicon tracker  
 48 consisted of 1856 silicon pixel and 15 148 silicon strip detector modules.

49 In the region  $|\eta| < 1.74$ , the HCAL cells have widths of 0.087 in pseudorapidity and 0.087  
 50 in azimuth ( $\phi$ ). In the  $\eta$ - $\phi$  plane, and for  $|\eta| < 1.48$ , the HCAL cells map on to  $5 \times 5$  arrays  
 51 of ECAL crystals to form calorimeter towers projecting radially outwards from close to the  
 52 nominal interaction point. For  $|\eta| > 1.74$ , the coverage of the towers increases progressively  
 53 to a maximum of 0.174 in  $\Delta\eta$  and  $\Delta\phi$ . The hadron forward (HF) calorimeter uses steel as an  
 54 absorber and quartz fibers as the sensitive material. The two halves of the HF are located 11.2 m  
 55 from the interaction region, one on each end, and together they provide coverage in the range  
 56  $3.0 < |\eta| < 5.2$ .

57 Events of interest are selected using a two-tiered trigger system. The first level (L1), composed  
 58 of custom hardware processors, uses information from the calorimeters and muon detectors to  
 59 select events at a rate of around 100 kHz within a fixed latency of about  $4 \mu\text{s}$  [8]. The second  
 60 level, known as the high-level trigger (HLT), consists of a farm of processors running a version  
 61 of the full event reconstruction software optimized for fast processing, and reduces the event  
 62 rate to around 1 kHz before data storage [9].

63 A more detailed description of the CMS detector, together with a definition of the coordinate  
 64 system used and the relevant kinematic variables, can be found in Ref. [10].

65 The candidate vertex with the largest value of summed physics-object transverse momenta  $p_T^2$   
 66 is taken to be the primary vertex (PV) of the pp interaction. The physics objects are the jets,  
 67 clustered using the jet finding algorithm [11, 12] with the tracks assigned to candidate vertices  
 68 as inputs, and the associated  $p_T^{\text{miss}}$ , taken as the negative vector sum of the  $p_T$  of those jets.

69 A particle-flow (PF) algorithm [13] aims to reconstruct and identify each individual particle in  
 70 an event, with an optimized combination of information from the various elements of the CMS  
 71 detector. In this process, the identification of the PF candidate type (photon, electron, muon,  
 72 and charged and neutral hadrons) plays an important role in the determination of the particle  
 73 direction and energy. The energy of photons is obtained from the ECAL measurement. The  
 74 energy of electrons is determined from a combination of the electron momentum at the PV as  
 75 determined by the tracker, the energy of the corresponding ECAL cluster, and the energy sum  
 76 of all bremsstrahlung photons spatially compatible with originating from the electron track.  
 77 The energy of muons is obtained from the curvature of the corresponding track. The energy of  
 78 charged hadrons is determined from a combination of their momentum measured in the tracker  
 79 and the matching ECAL and HCAL energy deposits, corrected for the response function of the

80 calorimeters to hadronic showers. Finally, the energy of neutral hadrons is obtained from the  
 81 corresponding corrected ECAL and HCAL energies.

82 The missing transverse momentum vector  $\vec{p}_T^{\text{miss}}$  is computed as the negative vector sum of  
 83 the transverse momenta of all the PF candidates in an event, and its magnitude is denoted as  
 84  $p_T^{\text{miss}}$ . The  $\vec{p}_T^{\text{miss}}$  is modified to account for corrections to the energy scale and resolution of  
 85 the reconstructed jets in the event [14]. Anomalous high- $p_T^{\text{miss}}$  events can be due to a variety  
 86 of reconstruction failures, detector malfunctions, or noncollision backgrounds. Such events  
 87 are rejected by dedicated filters that are designed to eliminate more than 85–90% of the spuri-  
 88 ous high- $p_T^{\text{miss}}$  events with a signal efficiency exceeding 99.9% [14]. For each event, hadronic  
 89 jets are clustered from the PF candidates using the infrared- and collinear-safe anti- $k_T$  algo-  
 90 rithm [11, 12] with a distance parameter of 0.4 or 1.5. Depending on the respective distance  
 91 parameter, these jets are referred to as “AK4” or “AK15” jets. Jet momentum is determined  
 92 as the vectorial sum of all particle momenta in the jet, and is found from simulation to be, on  
 93 average, within 5 to 10% of the true momentum over the entire  $p_T$  spectrum and detector accep-  
 94 tance [15]. Additional pp interactions within the same or nearby bunch crossings (pileup) can  
 95 contribute additional tracks and calorimetric energy depositions to the jet momentum. To mit-  
 96 iate this effect, charged particles identified as not originating from the PV are discarded and  
 97 an offset correction is applied to correct for the remaining neutral pileup contributions [15].  
 98 Jet energy corrections are derived from simulation to bring the measured response of jets to  
 99 that of particle-level jets on average. In situ measurements of the momentum balance in the  
 100 dijet,  $\gamma + \text{jet}$ ,  $Z + \text{jet}$ , and multijet events are used to account for any residual differences in  
 101 the jet energy scale (JES) and jet energy resolution (JER) in data and simulation [15]. The jet  
 102 energy resolution amounts typically to 15–20% at 30 GeV, 10% at 100 GeV, and 5% at 1 TeV [15].  
 103 Additional selection criteria [16] are applied to each jet to remove jets potentially dominated  
 104 by anomalous contributions from various subdetector components or reconstruction failures.  
 105 Narrow AK4 jets are also required to pass quality criteria based on the composition of the jet in  
 106 terms of different types of PF candidates, such as a minimum charged-hadron energy fraction  
 107 of 10% and a maximum neutral-hadron energy fraction of 80% [16].

108 Large-radius AK15 jets are used for the identification of the decays of the dark Higgs boson into  
 109 a b-quark pair. The pileup-per-particle identification (PUPPI) algorithm [17] is used to mitigate  
 110 the effect of pileup at the reconstructed-particle level, making use of local shape information,  
 111 event pileup properties, and tracking information. Charged particles identified as not originat-  
 112 ing from the PV are discarded. For each neutral particle, a local shape variable is computed  
 113 using the surrounding charged particles within the tracker acceptance ( $|\eta| < 2.5$ ) compatible  
 114 with the PV, and using both charged and neutral particles in the region outside of the tracker  
 115 coverage. The momenta of the neutral particles are then rescaled according to their probability  
 116 to originate from the PV deduced from the local shape variable, avoiding the need for jet-based  
 117 pileup corrections [16]. The modified mass drop tagger algorithm [18, 19], also known as the  
 118 soft-drop (SD) algorithm, with the angular exponent  $\beta = 0$ , soft cutoff threshold  $z_{\text{cut}} < 0.1$ , and  
 119 characteristic radius  $R_0 = 1.5$  [20], is applied to remove soft, wide-angle radiation from the jet.

## 120 2 Simulated samples

121 Monte Carlo (MC) simulated event samples are used to model signal and background contribu-  
 122 tions to all the analysis regions. In all cases, parton showering, hadronization, and underlying  
 123 event properties are modeled using PYTHIA [21] version 8.202 or later with the underlying  
 124 event tune CUETP8M1 or CP5 [22], based on the year of data taking. Simulation of inter-  
 125 actions between particles and the CMS detector is based on GEANT4 [23]. The NNPDF 3.0

126 next-to-next-to-leading order (NNLO) [24] and the NNPDF 3.1 NNLO [25] parton distribution  
 127 functions (PDFs) are used for the generation of all samples based on the year of data taking.  
 128 The same reconstruction algorithms used for data are applied to simulated samples.

129 For the V + jets processes, predictions with up to two partons in the final state are obtained  
 130 at leading order (LO) in QCD using MADGRAPH5\_aMC@NLO [26] with the MLM matching  
 131 scheme [27] between the jets from the matrix element calculations and the parton shower. Sam-  
 132 ples of events with top quark pairs are generated at next-to-leading (NLO) in QCD with up to  
 133 two additional partons in the matrix element calculations using MADGRAPH5\_aMC@NLO and  
 134 the FxFx jet matching scheme [28]. Their cross sections are normalized to the inclusive cross  
 135 section of the top quark pair production at NNLO in QCD [29]. Events with single top quarks  
 136 are simulated using POWHEG 2.0 [30, 31] and normalized to the inclusive cross section calcu-  
 137 lated at NLO in QCD [32, 33]. Production of diboson events (WW, WZ, and ZZ) is simulated  
 138 at NLO in QCD using PYTHIA, and normalized to the cross sections at NNLO precision for  
 139 WW production [34] and at NLO precision for the others [35]. Several production mechanisms  
 140 of the SM Higgs boson decaying into a bottom-quark pair are also produced at LO with the  
 141 POWHEG generator. Samples of QCD multijet production events are generated at LO using  
 142 MADGRAPH5\_aMC@NLO.

143 The MC samples for the dark Higgs boson signal process are generated with the MADGRAPH5\_aMC@NLO  
 144 with up to one additional parton in the matrix element calculations at LO with the MLM match-  
 145 ing scheme. The values of the vector coupling  $g_q$  between the Z' mediator and the quarks, as  
 146 well as the axial coupling  $g_\chi$  between the mediator and DM particles, are set to  $g_q = 0.25$  and  
 147  $g_\chi = 1.0$ , respectively, as recommended by the LHC Dark Matter Working Group [36]. Separate  
 148 samples are generated for different mass hypotheses for the mediator, DM particles, and dark  
 149 Higgs boson.

### 150 3 Event selection

151 The key feature of the analysis is the extensive use of control data samples for the purpose of  
 152 precise prediction of the background contributions in the signal regions (SRs), which contain  
 153 events with a large-radius, high- $p_T$  jet and large  $p_T^{\text{miss}}$ . The leading SM background contribu-  
 154 tions originate from  $Z \rightarrow \nu\nu$  and  $W \rightarrow \ell\nu$  production ( $\ell = e, \mu, \tau$ ), the properties of which  
 155 are constrained using control regions (CRs) with zero or one charged lepton, that are enriched  
 156 in  $Z \rightarrow \nu\nu$  and  $W \rightarrow \ell\nu$  events, respectively. Additionally, CRs enriched in  $t\bar{t}$  production  
 157 events are also defined. The V + jets and  $t\bar{t}$  production events in these CRs share many kine-  
 158 matic properties of the processes in the SRs and are used to constrain the latter. The CR and SR  
 159 definitions share as many of the selection criteria as possible, in order to ensure that minimal  
 160 selection biases are introduced. Seven CRs are defined: six single-electron and single-muon  
 161 CRs enriched in  $W \rightarrow \ell\nu$  and  $t\bar{t}$  production events, and a seventh CR enriched in  $Z \rightarrow \nu\nu$   
 162 production events.

163 The SR events are selected using a trigger with a  $p_T^{\text{miss}}$  requirement of at least 120 GeV. The  
 164 trigger requirement for the SRs is based on an online calculation of  $p_T^{\text{miss}}$  based on all PF can-  
 165 didates reconstructed at the HLT, except for muons. Events with high- $p_T$  muons are there-  
 166 fore also assigned large online  $p_T^{\text{miss}}$ , and the same trigger is used to collect data populating  
 167 the single-muon and CRs. The control samples with electrons are selected based on two dif-  
 168 ferent single-electron triggers requiring of  $p_T > 27$  (35, 32) GeV for 2016 (2017, 2018) and  
 169  $p_T > 105$  GeV (115) for 2016 (2017 and 2018), and on a single-photon trigger with a require-  
 170 ment of  $p_T > 200$  GeV (for 2017 and 2018 only). The single-electron triggers differ in their  
 171 usage of isolation requirements: while the lower threshold trigger requires electrons to be well

isolated, the higher-threshold trigger does not, which gives an improved efficiency at high  $p_T$ . Similarly, the single-photon trigger avoids the reliance on the online track reconstruction and increases the overall efficiency for electrons with  $p_T > 200 \text{ GeV}$ . During the 2016 and 2017 data taking, a gradual shift in the timing of the inputs of the ECAL L1 trigger in the region at  $|\eta| > 2.0$  caused a specific trigger inefficiency. For events containing an electron or a photon (a jet) with  $p_T \gtrsim 50$  (100)  $\text{GeV}$  in this region, the efficiency loss is up to  $\approx 10\text{--}20\%$ , depending on  $p_T$ ,  $\eta$ , and time. This issue is known as the L1 pre-firing. Correction factors are computed from data and applied to the acceptance evaluated by simulation for the 2016 and 2017 samples.

At the analysis level, a requirement of  $p_T^{\text{miss}} > 250 \text{ GeV}$  is applied to the SR events in order to ensure a  $p_T^{\text{miss}}$  trigger efficiency of at least 95%. The leading AK15 jet in  $p_T$  is required to have  $p_T > 160 \text{ GeV}$ ,  $|\eta| < 2.4$ , an SD-corrected mass ( $m_{\text{SD}}$ ) of  $40 < m_{\text{SD}} < 300 \text{ GeV}$ . In order to preferentially select events where the leading AK15 jet originates from a hadronic decay of a dark Higgs boson, the jet is further required to be double-b tagged with the DEEPAK15 algorithm [37]. The DEEPAK15 algorithm employs a deep neural network to differentiate between jets from vector boson, top quark, and Higgs boson decays, as well as jets originating from QCD radiation. The inputs to the neural network are features of up to 100 jet constituent PF candidates of a given jet and features related to up to seven secondary vertices reconstructed in a given collision event. For each jet, the output of the neural network is one numerical score for each of the jet classes, representing the likelihood that the jet originates from that class. In this analysis, separation between dark Higgs bosons and QCD jets is sought, and a binary score is constructed by taking the ratio of the sum of the SM  $Z \rightarrow bb$  and  $H \rightarrow bb$  scores to the sum of the SM  $Z \rightarrow bb$ ,  $H \rightarrow bb$ , and QCD scores.

Further requirements are imposed in order to suppress reducible background processes. Events are rejected if they contain a well-reconstructed and isolated electron (photon) with  $p_T > 10$  (15)  $\text{GeV}$  and  $|\eta| < 2.5$  or a muon with  $p_T > 10 \text{ GeV}$  and  $|\eta| < 2.4$  [38, 39]. Hadronically decaying  $\tau$  leptons are identified using the DEEPTAU algorithm [40]. Events with a hadronically decaying  $\tau$  lepton candidate with  $p_T > 20 \text{ GeV}$  and  $|\eta| < 2.3$  are removed. These requirements efficiently reject events with leptonic decays of the V bosons and top quarks, as well as backgrounds with photons. Contributions from top quark processes are further suppressed by rejecting events with AK4 jets that do not overlap with the leading AK15 jet, have  $p_T > 20 \text{ GeV}$  and  $|\eta| < 2.4$ , and are identified to have originated from the hadronization of a bottom quark (“b-tagged jets”). The b-tagging of AK4 jets is performed using the DEEPJET algorithm [41] with a “loose” working point, corresponding to a probability of 10% of misidentifying a light-flavor quark or gluon jet. Finally, topological requirements are applied in order to reject contributions from QCD multijet events. These events do not have  $p_T^{\text{miss}}$  from genuine sources and require a  $p_T^{\text{miss}}$  mismeasurement in order to pass the SR selections, which can happen in two main ways. In the first case, the energy of a jet in the event could be misreconstructed either as a result of an interaction between the jet with poorly instrumented or inactive parts of the detector, or because of failures in the readout of otherwise functioning detector modules. In these cases, artificial  $p_T^{\text{miss}}$  is generated with a characteristically small azimuthal angle difference between the misreconstructed jet  $\vec{p}_T$  and the  $\vec{p}_T^{\text{miss}}$  vectors. Such events are rejected by requiring the minimum azimuthal angle between the  $\vec{p}_T^{\text{miss}}$  direction and each AK4 jet in the event to be larger than 0.5 radians. With the same goal, the azimuthal angle between the  $\vec{p}_T^{\text{miss}}$  direction and each AK15 jet in the event must be larger than 1.5 radians. In the second case, large  $p_T^{\text{miss}}$  is generated due to failures of the PF reconstruction, which are suppressed by considering an alternative calculation of  $p_T^{\text{miss}}$  based on calorimeter energy clusters and muon candidates, rather than the full set of all PF candidates. While the calorimeter-based  $p_T^{\text{miss}}$  has significantly worse resolution than PF  $p_T^{\text{miss}}$ , it is much simpler and more robust. To re-

duce the multijet background caused by PF reconstruction failures, events are required to have  $\Delta p_T^{\text{miss}}(\text{PF-calorimeter}) = |p_T^{\text{miss}}(\text{PF})/p_T^{\text{miss}}(\text{calorimeter}) - 1| < 0.5$ . Finally, a section of the HCAL was not functioning during a part of the 2018 data taking period corresponding to 65% of the total integrated luminosity recorded in that year, leading to irrecoverable mismeasurement in a localized region of the detector ( $-1.57 < \phi < -0.87, -3.0 < \eta < -1.3$ ). To avoid contamination from such mismeasurement, events where any jet with  $p_T > 30 \text{ GeV}$  is found in the corresponding  $\eta$ - $\phi$  region are rejected in the analysis of the 2018 data set. Events where the mismeasurement is so severe that a jet is fully lost in this region are found to contribute at low values of  $p_T^{\text{miss}} < 470 \text{ GeV}$  and to have a characteristic signature in  $\phi(\vec{p}_T^{\text{miss}})$ . Such events are rejected by requiring that  $\phi(\vec{p}_T^{\text{miss}}) \notin [-1.62, -0.62]$  if  $p_T^{\text{miss}} < 470 \text{ GeV}$ . Expected yields from different processes in SR are reported in Table 1.

Table 1: Expected yields from background processes in the signal region for different years of data taking. Uncertainties are statistical-only.

	2016	2017	2018
H $\rightarrow b\bar{b}$	$57.6 \pm 0.3$	$72.0 \pm 0.3$	$83.8 \pm 0.3$
Z( $\rightarrow \ell\ell$ )+jets	$19.3 \pm 0.7$	$43.3 \pm 2.0$	$37.1 \pm 3.0$
QCD multijet	$93.3 \pm 25.8$	$154.9 \pm 41.7$	$163.2 \pm 64.6$
Diboson	$718.0 \pm 17.5$	$623.4 \pm 17.8$	$606.4 \pm 20.8$
Single t	$646.0 \pm 10.9$	$567.4 \pm 12.5$	$614.6 \pm 12.8$
t $\bar{t}$	$5486.5 \pm 199.7$	$5810.0 \pm 60.0$	$6784.2 \pm 133.7$
W( $\rightarrow \ell\nu$ )+jets	$3997.9 \pm 38.5$	$2991.0 \pm 40.2$	$2826.6 \pm 50.5$
Z( $\rightarrow \nu\nu$ )+jets	$7514.9 \pm 29.2$	$7035.1 \pm 33.3$	$6978.5 \pm 38.8$
Total expected	$18533.4 \pm 208.1$	$17297.2 \pm 92.4$	$18094.2 \pm 163.4$

A control region (labelled as “ZCR”) composed of those events that satisfy all the SR requirements, but have the leading AK15 jet failing the DEEPAK15 selection, is used to constrain Z( $\nu\nu$ ) + jets production in SR. Single-lepton CRs (labelled as “WEPCR” and “WMPCR”) are used to constrain W( $\ell\nu$ ) + jets events in SR. The same selection criteria are applied to these CRs as for the SR, with the exception of the charged-lepton rejection criteria being inverted to allow for exactly one muon or one electron. The  $\vec{p}_T^{\text{miss}}$  vector used in the SR definition is replaced by the hadronic recoil vector  $\vec{U}$ . The hadronic recoil is defined as the vectorial sum of the  $\vec{p}_T^{\text{miss}}$  vector and the transverse momentum vectors of the selected charged lepton in each event. The hadronic recoil therefore acts as a proxy of the momentum of the W boson in each CR, convolved with the  $p_T^{\text{miss}}$  resolution, which is equivalent to the role of  $p_T^{\text{miss}}$  in the SR. In order to enhance the purity of the CRs, specific additional selection criteria are applied. For the charged-lepton CRs, at least one of the leptons is required to pass a more strict set of quality criteria and have  $p_T > 40$  (20) GeV electrons (muons). Additionally, in the single-electron CR are required to have  $p_T^{\text{miss}} > 100$  GeV in order to reject contributions from QCD multijet events. Additional single-lepton CRs (labelled as “WEFCR” and “WMFCR”) composed of those single-lepton events with the leading AK15 jet failing the DEEPAK15 selection are also used to constrain W( $\ell\nu$ ) + jets events in SR. Finally, in order to select single-lepton events enriched in t $\bar{t}$  production, additional CRs (labelled as “TECR” and “TMCR”) are identified by inverting the veto on b-tagged AK4 jets outside the leading AK15 jet cone.

The selection criteria that define the different SR and CRs are summarized in Table 2.

Table 2: Summary of cuts that define the different analysis regions.

Selection	SR	ZCR	WMPCR	WEPCR	WMFCR	WEFCR	TTMCR	TTECR
$U > 250 \text{ GeV}$	✓	✓	✓	✓	✓	✓	✓	✓
$\Delta p_T^{\text{miss}}(\text{PF-calorimeter}) > 0.5$	✓	✓	✓	✓	✓	✓	✓	✓
Leading AK15 $p_T > 160 \text{ GeV}$	✓	✓	✓	✓	✓	✓	✓	✓
Leading AK15 $m_{SD} \in [40, 300] \text{ GeV}$	✓	✓	✓	✓	✓	✓	✓	✓
$\min \Delta\phi(\vec{U}, A\vec{K}4s) > 0.5$	✓	✓	✓	✓	✓	✓	✓	✓
$\min \Delta\phi(\vec{U}, A\vec{K}15s) > 1.5$	✓	✓	✓	✓	✓	✓	✓	✓
$p_T^{\text{miss}} > 100 \text{ GeV}$	✗	✗	✗	✓	✗	✓	✗	✓
# of muons	0	0	1	0	1	0	1	0
# of electrons	0	0	0	1	0	1	0	1
# of photons	0	0	0	0	0	0	0	0
# of taus	0	0	0	0	0	0	0	0
# of extra b-tagged AK4s	0	0	0	0	0	0	$\geq 1$	$\geq 1$
DeepAK15 > wp(90% signal eff.)	pass	fail	pass	pass	fail	fail	pass	pass

## 251 4 Background estimation

252 Background estimation and signal extraction are performed simultaneously, using a joint maximum  
 253 likelihood (ML) fit across all SR and CRs. A likelihood function is constructed to model  
 254 the expected background contributions in each bin of the two-dimensional recoil-vs- $m_{SD}$  vari-  
 255 able of the SR and CRs, as well as the expected signal yield in each bin of the SR. The best fit  
 256 background model, as well as the best fit signal strength, are obtained by maximizing the joint  
 257 likelihood function of all categories.

### 258 4.1 Likelihood function

259 The likelihood function maximized by the fit is:

$$\begin{aligned}
\mathcal{L}_c(\mu_{ZCR}^Z, \mu_{SR}^{t\bar{t}}, \mu, \theta) = & \prod_{i,j} \text{Poisson} \left( d_{i,j}^{ZCR} | B_{i,j}^{ZCR}(\theta) + (1 + R^{W-Z})_{i,j}(\theta) \mu_{ZCR,i,j}^Z \right) \\
& \times \prod_{i,j} \text{Poisson} \left( d_{i,j}^{TTECR} | B_{i,j}^{TTECR}(\theta) + \frac{\mu_{SR,i,j}^{t\bar{t}}}{R_{TTECR,i,j}^{t\bar{t}}(\theta)} \right) \\
& \times \prod_{i,j} \text{Poisson} \left( d_{i,j}^{TTMCR} | B_{i,j}^{TTMCR}(\theta) + \frac{\mu_{SR,i,j}^{t\bar{t}}}{R_{TTMCR,i,j}^{t\bar{t}}(\theta)} \right) \\
& \times \prod_{i,j} \text{Poisson} \left( d_{i,j}^{WEFCR} | B_{i,j}^{WEFCR}(\theta) + \frac{R^{W-Z}_{i,j}(\theta) \mu_{ZCR,i,j}^Z}{R_{WEFCR,i,j}^W(\theta)} \right) \\
& \times \prod_{i,j} \text{Poisson} \left( d_{i,j}^{WMFCR} | B_{i,j}^{WMFCR}(\theta) + \frac{R^{W-Z}_{i,j}(\theta) \mu_{ZCR,i,j}^Z}{R_{WMFCR,i,j}^W(\theta)} \right) \\
& \times \prod_{i,j} \text{Poisson} \left( d_{i,j}^{WEPCR} | B_{i,j}^{WEPCR}(\theta) + \frac{R_{p/f,i,j}^W(\theta) R^{W-Z}_{i,j}(\theta) \mu_{ZCR,i,j}^Z}{R_{WEPCR,i,j}^W(\theta)} + \frac{\mu_{SR,i,j}^{t\bar{t}}}{R_{WEPCR,i,j}^{t\bar{t}}(\theta)} \right) \\
& \times \prod_{i,j} \text{Poisson} \left( d_{i,j}^{WMPCR} | B_{i,j}^{WMPCR}(\theta) + \frac{R_{p/f,i,j}^W(\theta) R^{W-Z}_{i,j}(\theta) \mu_{ZCR,i,j}^Z}{R_{WMPCR,i,j}^W(\theta)} + \frac{\mu_{SR,i,j}^{t\bar{t}}}{R_{WMPCR,i,j}^{t\bar{t}}(\theta)} \right) \\
& \times \prod_i \text{Poisson} \left( d_{i,j}^{SR} | B_{i,j}^{SR}(\theta) + (R_{p/f,i,j}^Z(\theta) + R_{p/f,i,j}^W(\theta) R^{W-Z}_{i,j}(\theta)) \mu_{ZCR,i,j}^Z + \mu_{SR,i,j}^{t\bar{t}} + \mu S_{i,j}(\theta) \right)
\end{aligned} \tag{1}$$

260 In the above likelihood,  $d_{i,j}^{*R}$  are the observed number of events in each  $(i,j)$  bin of the two-  
261 dimensional recoil-vs- $m_{SD}$  distribution in the SR and CRs, while  $B_{i,j}^{*R}$  is the number of back-  
262 ground events. The parameter  $\mu_{ZCR}^Z$  represents the yield of the  $Z \rightarrow \nu\nu + \text{jets}$  background in  
263 the ZCR, and is left freely floating in the fit. The parameter  $\mu_{SR}^{t\bar{t}}$  represents the yield of the  $t\bar{t}$   
264 background in the SR, that is left freely floating in the fit as well. The likelihood also includes  
265 the SR with  $\mu$  being the signal strength parameter also left floating in the fit. The systematic  
266 uncertainties ( $\theta$ ) enter the likelihood as additive perturbations to the transfer factors  $R$  used in  
267 the modeling of the main backgrounds, as well as to the minor background and signal expec-  
268 tations, and are modeled as Gaussians.

269 Separate approaches are adopted to estimate the dominant ( $Z + \text{jets}$ ,  $W + \text{jets}$ ,  $t\bar{t}$ ) and subdom-  
270 inant (single top, diboson, Higgs, and QCD multijet) backgrounds.

271 The predictions for the dominant  $Z + \text{jets}$  and  $W + \text{jets}$  backgrounds are based on the yield of  
272  $Z \rightarrow \nu\nu$  events in each bin of the ZCR. The per-bin yields for this process are defined as free  
273 parameters of the likelihood function. The yields for the  $Z + \text{jets}$  and  $W + \text{jets}$  contribution  
274 to the SR, as well as the yields of the  $W + \text{jets}$  process in the CRs are defined relative to the  
275  $Z \rightarrow \nu\nu$  yields by introducing a set of per-bin transfer factors. The yields of  $t\bar{t}$  events in the  
276 single-lepton CRs are similarly related via transfer factors to the  $t\bar{t}$  event yields in the SRs. This  
277 choice of transfer factors takes into account the correlations between the  $V + \text{jets}$  background  
278 contributions in all regions. In all cases, the central values of the transfer factors are obtained  
279 from the ratios of the simulated recoil-vs- $m_{SD}$  spectra of the respective processes in the SRs to

280 those in CRs. For the minor backgrounds the nominal expected yield per region is obtained  
281 directly from simulation.

282 Systematic uncertainties are incorporated in the likelihood function as nuisance parameters,  
283 as described in more detail below. In the case of the  $V + \text{jets}$  and  $t\bar{t}$  processes, the nuisance  
284 parameters affect the values of the transfer factors in each recoil-vs- $m_{\text{SD}}$  variable bin and thus  
285 control the ratios of the contributions from different processes, as well as the ratios of the yields  
286 in the SRs to those in various CRs. For the subdominant background processes, the yields in  
287 each bin are directly parameterized in terms of the nuisance parameters. The final free pa-  
288 rameter of the likelihood function is the signal strength modifier  $\mu$ , which—for a given signal  
289 hypothesis—controls the signal normalization relative to the theoretical cross section.

290 The likelihood method relies on the accurate predictions of the ratios between the dominant  
291 backgrounds in the SRs and CRs, as well as on the absolute normalization and shape of the  
292 recoil-vs- $m_{\text{SD}}$  distributions for the subdominant backgrounds. To achieve the most accurate  
293 possible predictions for these quantities, weights are applied to each simulated event to take  
294 into account both experimental and theoretical effects not present in the MC simulated sam-  
295 ples. The experimental corrections are related to the trigger efficiencies, identification and  
296 reconstruction efficiencies of charged leptons and of b-tagged and doubleb-tagged jets, and  
297 the pileup distribution in simulation. Theoretical corrections are applied to the  $V + \text{jets}$  pro-  
298 cesses in order to model the effects of NLO terms in the perturbative EW corrections [42]. The  
299 corrections are parameterized as functions of the generator-level boson  $p_{\text{T}}$  and are evaluated  
300 separately for the  $W(\ell\nu) + \text{jets}$  and  $Z(\ell\ell) + \text{jets}$  processes.

## 301 **4.2 Systematic uncertainties**

302 The inputs to the ML fit are subject to various experimental and theoretical uncertainties. Un-  
303 certainties in the measurement of the integrated luminosity in each year of data taking are  
304 0.6–2%. The uncertainties in the corrections for the L1 pre-firing effect in 2016 and 2017, as  
305 well as the uncertainties in the pile up correction are of the order of 1%. The uncertainties in  
306 the efficiencies of reconstructing and identifying electron candidates are 1% and 2–3%, respec-  
307 tively. For muons, the uncertainties in the identification efficiency are 1%, with an additional  
308 1% uncertainty in the efficiency of the isolation criteria. A systematic uncertainty for each lep-  
309 ton/photon veto selection has been obtained by propagating the overall uncertainties in the  
310 identification of muons, electrons, photons, and taus, into the vetoed regions. While the un-  
311 certainties are found to be negligible for photon, muon, and electron vetoes, a 3% uncertainty  
312 in the tau veto is included. The uncertainties in the trigger efficiency are 1% for the single  
313 electron trigger and 1–2% for the  $p_{\text{T}}^{\text{miss}}$  trigger. The uncertainty in the modeling of  $p_{\text{T}}^{\text{miss}}$  in sim-  
314 ulation [43] is dominated by the uncertainty in the jet energy corrections. The resulting bin  
315 migration affects the acceptance of the minimum requirement in  $p_{\text{T}}^{\text{miss}}$ . The change in rate is  
316 estimated to be 5% and it is included as a systematic uncertainty. An additional systematic un-  
317 certainty is included to cover the effect of the uncertainties in the AK15 jet energy corrections  
318 on the AK15 jet  $p_{\text{T}}$ . Also in this case, the resulting bin migration affects the acceptance of the  
319 minimum requirements in AK15 jet  $p_{\text{T}}$ . This introduces an effect on the rate of the order of 4%.  
320 The uncertainty in the b-tagging efficiency leads to a shape uncertainty applied to all processes  
321 in all regions. The uncertainty in the doubleb-tagging efficiency results in a shape uncertainty  
322 applied to the signal processes in SR. Uncertainties of 100% are assigned to the normalization  
323 of the QCD multijet background contributions in the all regions. These uncertainties are corre-  
324 lated between regions with the same source of fake: one uncertainty is applied to QCD multijet  
325 events in the SR and in the ZCR, a separate uncertainty is applied to QCD multijet events in the  
326 single-muon CRs, and similarly for the single-electron CRs. Additionally, uncertainties of 20%

are assigned to the cross section of diboson, SM Higgs boson, and  $Z(\rightarrow \ell\ell)$ +jets productions. Similarly, 10% uncertainties in the single top quark and  $t\bar{t}$  production cross sections are also assigned. The theoretical uncertainties in the transfer factors related to higher-order effects in the QCD and EW perturbative expansions are calculated according to the prescription given in Ref. [42] and implemented, as described in Ref. [44]. Bin-by-bin statistical uncertainties are incorporated following the Barlow-Beeston-lite approach [45].

The likelihood functions obtained for the three data taking years are combined in order to maximize the statistical power of the analysis. The combination is performed by defining a combined likelihood describing all the analysis regions in all data sets. For this purpose, the effects of all theoretical uncertainties are assumed to be correlated. Most experimental uncertainties are dominated by the inherent precision of auxiliary measurements specific to each data set and are thus assumed to be uncorrelated between different data taking years. The experimental uncertainties related to the determination of the integrated luminosity and to the b-tagging efficiency are partially correlated between the data taking years, which is taken into account by splitting the total uncertainty into its correlated and uncorrelated components.

## 5 Results and interpretation

The ML fit is performed by combining the analysis categories as well as the data sets corresponding to the different years of data taking. The recoil-vs- $m_{SD}$  distributions in SR and CRs before (“pre-fit”) and after (“post-fit”) the fit are shown in Figs. 2-16. In all cases, good agreement is observed between the background-only post-fit result and the data.

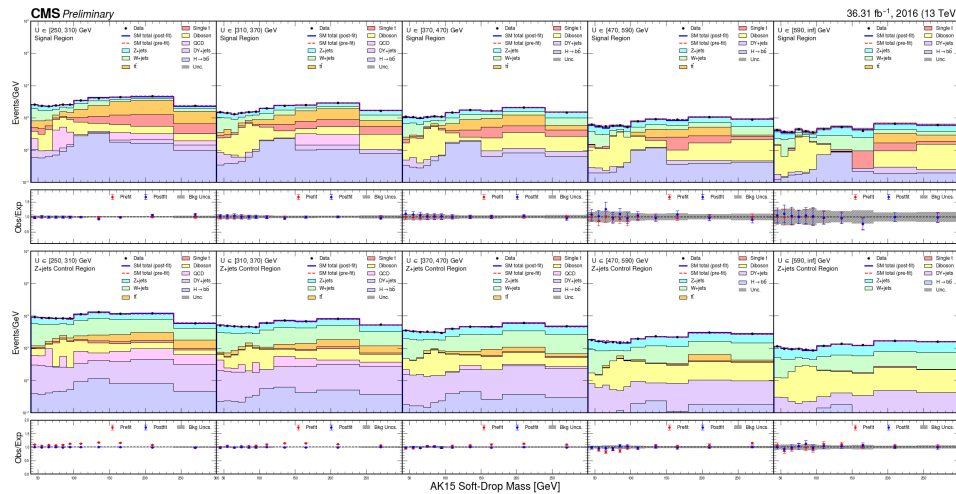


Figure 2: Post-fit  $m_{SD}$  distributions in bins of  $U$ . Top, distributions in signal region; bottom, distributions in  $Z$ +jets control region.

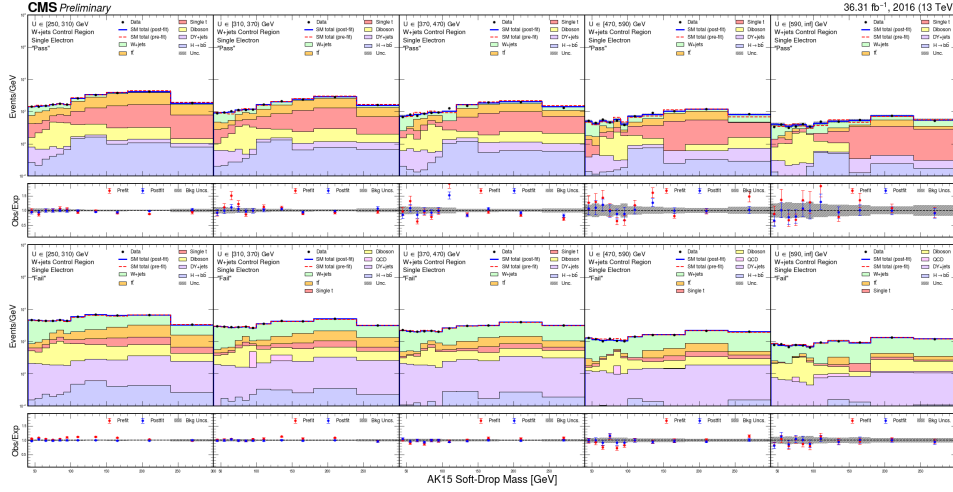


Figure 3: Post-fit  $m_{SD}$  distributions in bins of  $U$ . Top, distributions in W+jets single electron “pass” control region; bottom, distributions in W+jets single electron “fail” control region.

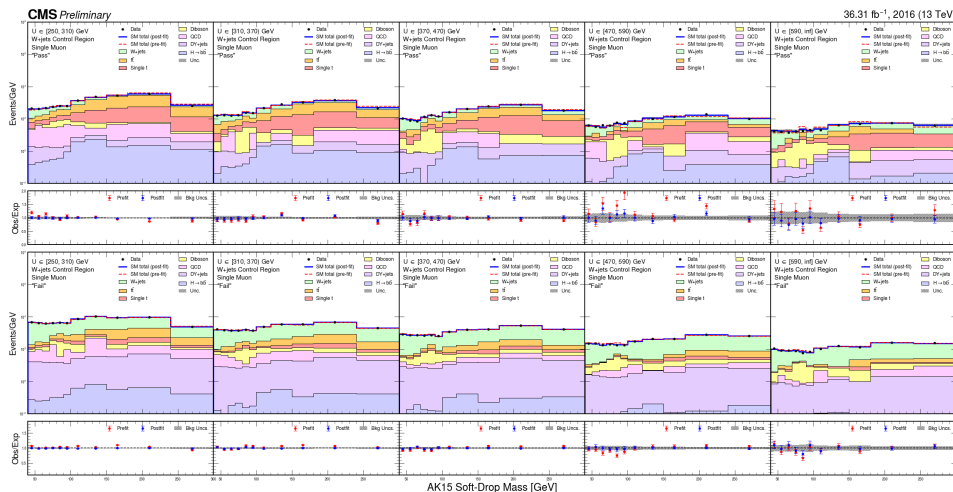


Figure 4: Post-fit  $m_{SD}$  distributions in bins of  $U$ . Top, distributions in W+jets single muon “pass” control region; bottom, distributions in W+jets single muon “fail” control region.

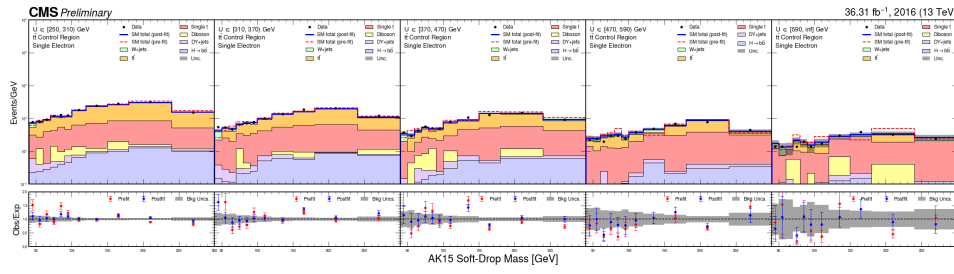


Figure 5: Post-fit  $m_{SD}$  distributions in bins of  $U$  in  $t\bar{t}$  single electron control region.

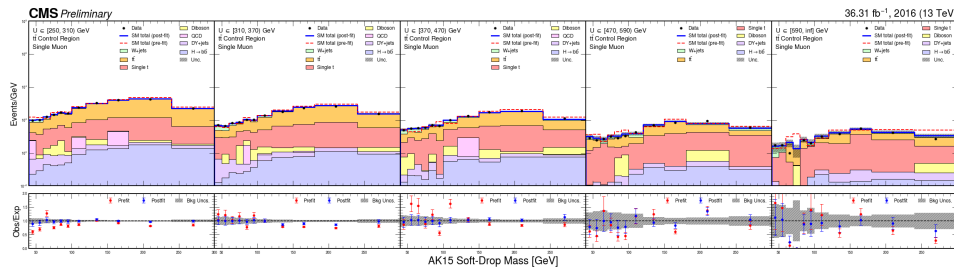


Figure 6: Post-fit  $m_{SD}$  distributions in bins of  $U$  in  $t\bar{t}$  single muon control region.

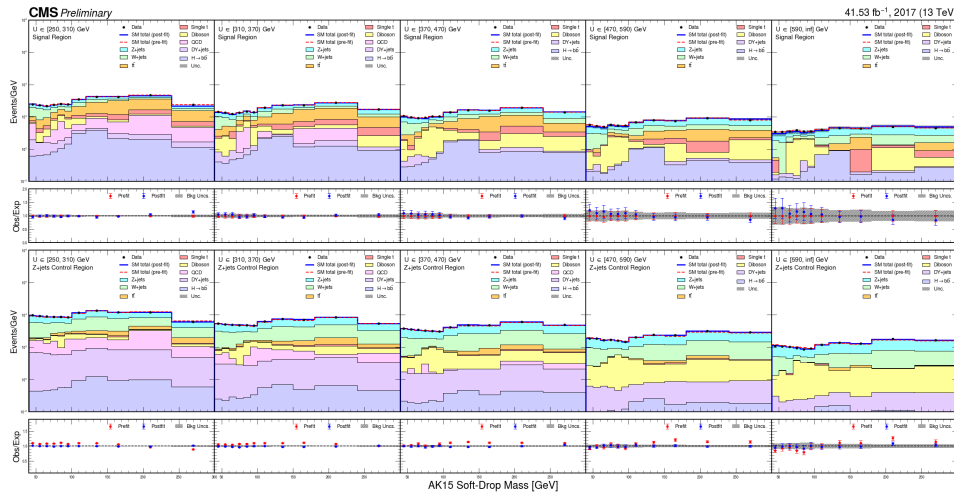


Figure 7: Post-fit  $m_{SD}$  distributions in bins of  $U$ . Top, distributions in signal region; bottom, distributions in Z+jets control region.

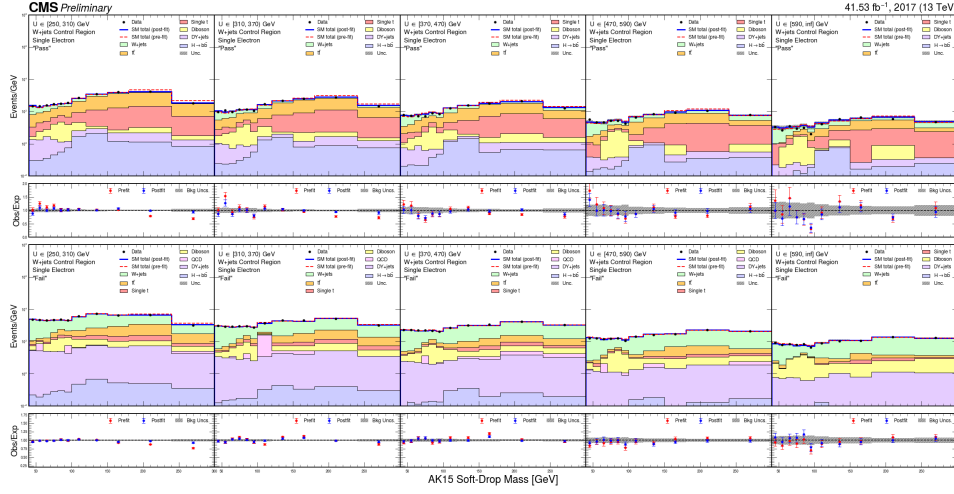


Figure 8: Post-fit  $m_{SD}$  distributions in bins of  $U$ . Top, distributions in W+jets single electron “pass” control region; bottom, distributions in W+jets single electron “fail” control region.

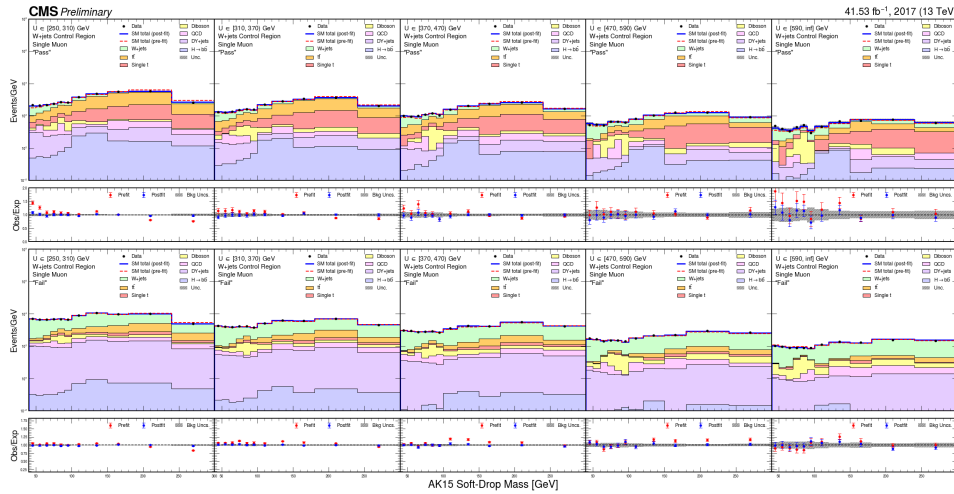


Figure 9: Post-fit  $m_{SD}$  distributions in bins of  $U$ . Top, distributions in W+jets single muon “pass” control region; bottom, distributions in W+jets single muon “fail” control region.

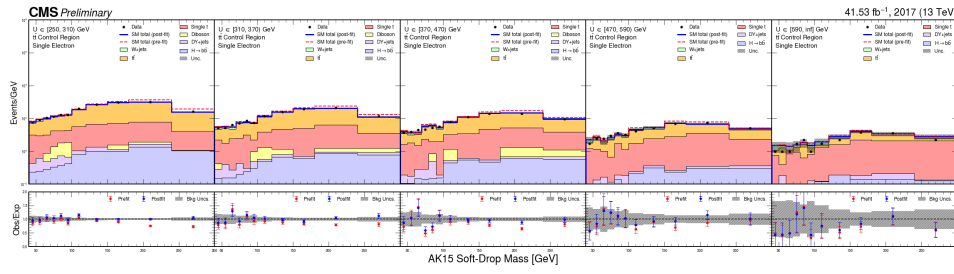


Figure 10: Post-fit  $m_{SD}$  distributions in bins of  $U$  in  $t\bar{t}$  single electron control region.

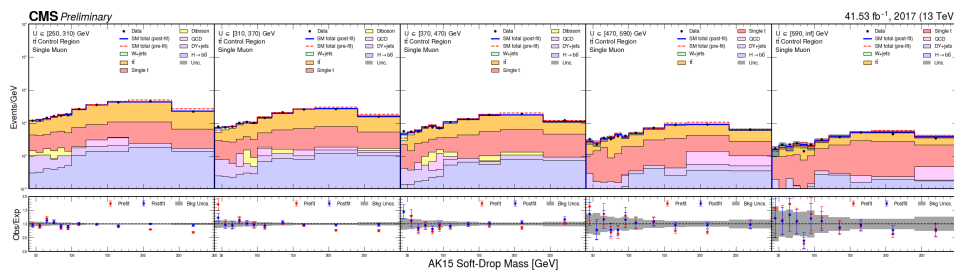


Figure 11: Post-fit  $m_{SD}$  distributions in bins of  $U$  in  $t\bar{t}$  single muon control region.

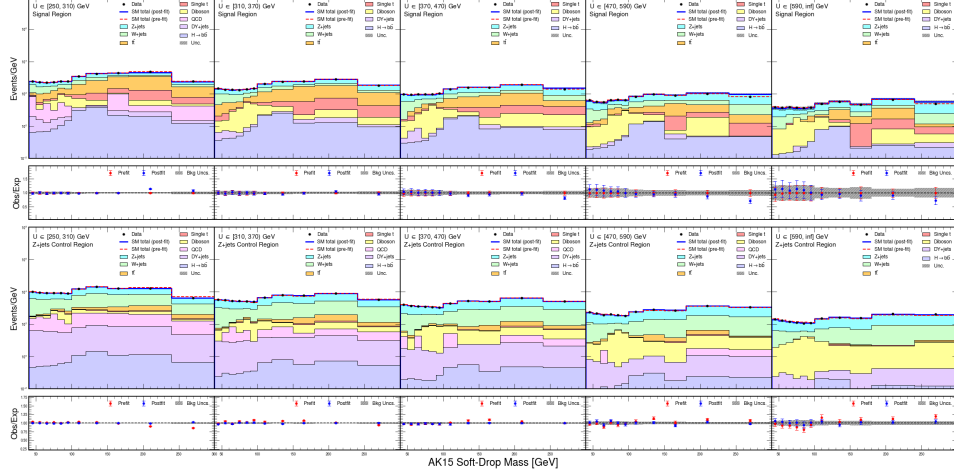


Figure 12: Post-fit  $m_{SD}$  distributions in bins of  $U$ . Top, distributions in signal region; bottom, distributions in  $Z+jets$  control region.

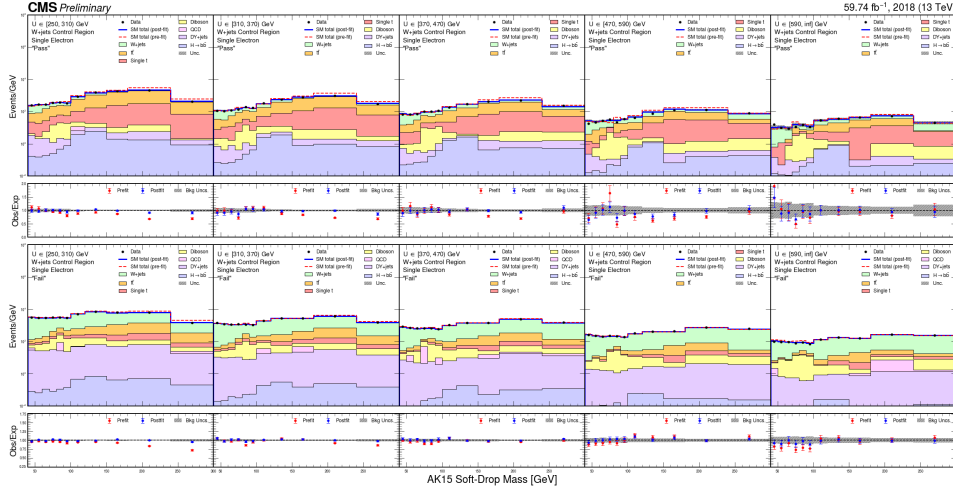


Figure 13: Post-fit  $m_{SD}$  distributions in bins of  $U$ . Top, distributions in W+jets single electron “pass” control region; bottom, distributions in W+jets single electron “fail” control region.

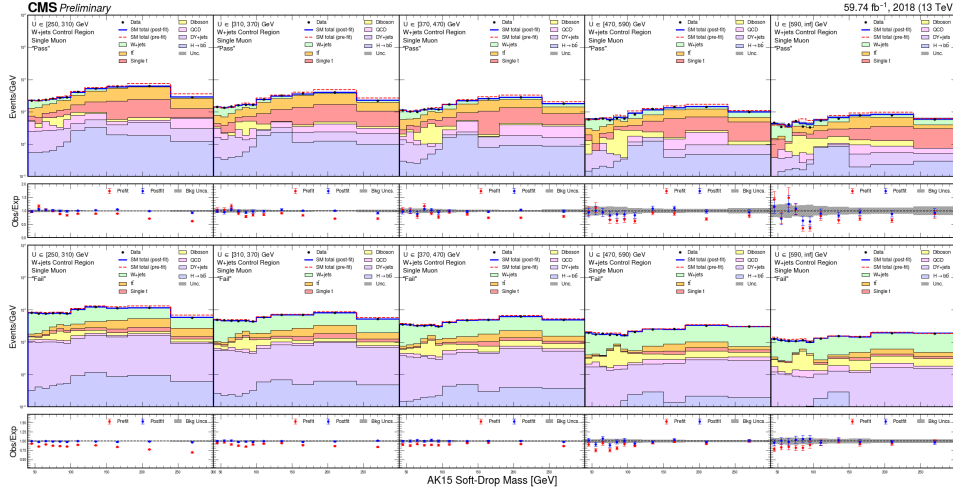


Figure 14: Post-fit  $m_{SD}$  distributions in bins of  $U$ . Top, distributions in W+jets single muon “pass” control region; bottom, distributions in W+jets single muon “fail” control region.

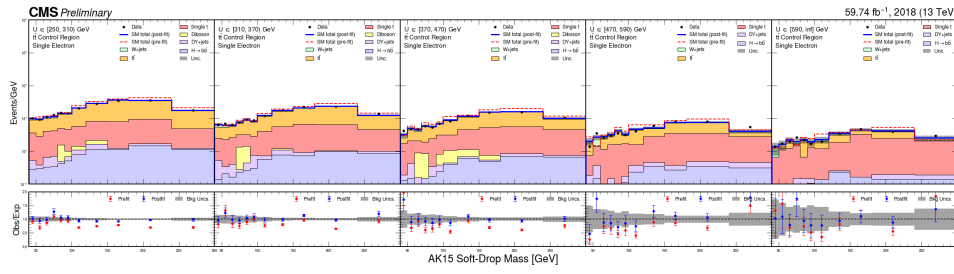


Figure 15: Post-fit  $m_{SD}$  distributions in bins of  $U$  in  $t\bar{t}$  single electron control region.

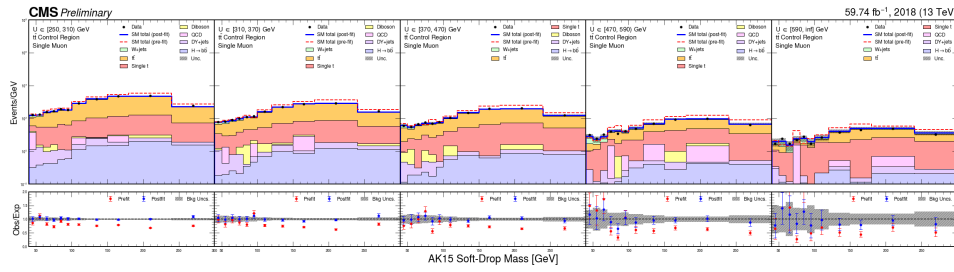


Figure 16: Post-fit  $m_{SD}$  distributions in bins of  $U$  in  $t\bar{t}$  single muon control region.

347 Signal strength exclusion limits are presented for different signal hypotheses. All data sets and  
 348 categories are included. The exclusion limits are calculated using the asymptotic approxima-  
 349 tion of the  $CL_s$  method [46–48]. In this method, a signal-plus-background fit is performed for  
 350 each signal hypothesis in addition to the background-only fit. In the signal fits, the nuisance  
 351 parameters are profiled, and the resulting best fit nuisance parameters vary for the different  
 352 signal hypotheses. Consequently, different nonzero best fit values for the signal strength can  
 353 be obtained for different signals even if the background-only fit succeeds in modeling the data.  
 354 In the exclusion limits, this feature is represented by differences between the observed and  
 355 expected limits.

356 Exclusion limits are calculated in the two-dimensional parameter space of the DM and medi-  
 357 ator masses,  $m_{DM}$  and  $m_{med}$ . The coupling between the mediator and SM quarks is set to a  
 358 constant value of  $g_q = 0.25$ , and the mediator-DM coupling is set to  $g_\chi = 1.0$ . The resulting  
 359 exclusion limits at 95% confidence level (CL) on the signal strength  $\mu$  are shown in Figs. 17–22  
 360 for different hypotheses of the dark Higgs boson mass. For small values of  $m_{DM} \approx 1$  GeV dif-  
 361 ferent values of the mediator mass  $m_{med}$  are expected to be excluded as a function of the dark  
 362 Higgs boson mass. The excluded value of  $m_{med}$  reduces with increasing values of  $m_{DM}$ , as the  
 363 branching fraction for decays of the mediator into dark matter candidates is reduced.

364 The constraints placed on the dark Higgs boson production model imply bounds on the inter-  
 365 action cross section between DM candidates and nuclei. The fixed-coupling exclusion curves at  
 366 90% CL in the  $m_{med}$ - $m_{DM}$  plane are translated point-by-point using the formulae described in  
 367 Ref. [49], which depend on the coupling choices  $g_q = 0.25$  and  $g_\chi = 1.0$  and on the specific sig-  
 368 nal model. The resulting curves in the  $m_{DM}$ - $\sigma_{DM\text{-nucleon}}$  plane are compared to the results from  
 369 DD experiments in Figs. 17–22. Qualitatively, although model dependent, the results from this  
 370 search depend on  $m_{DM}$  only weakly (as long as  $m_{DM} < m_{med}/2$ ), leading to stringent con-  
 371 straints also at low values of  $m_{DM}$ . The sensitivity of most DD experiments is limited in this

regime as the small value of  $m_{\text{DM}}$  translates into a reduced signal-to-noise ratio relative to the case of more massive DM. Depending on the mediator type, the resulting couplings between DM particles and nuclei are either spin dependent (axial-vector) or independent (vector). In the spin-dependent case, the sensitivity of DD experiments is limited relative to collider searches as the DM-nucleus scattering is no longer coherent.

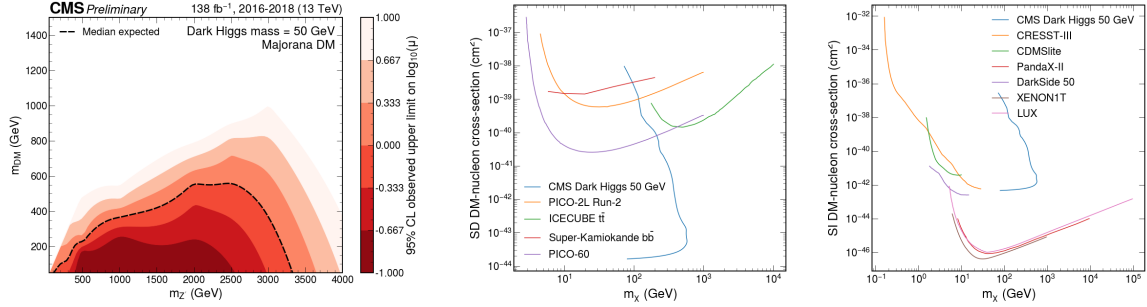


Figure 17: Left, expected exclusion limits at 95% CL on the signal strength  $\mu = \sigma/\sigma_{\text{theo}}$  as a function of  $m_{\text{med}}$  for a dark Higgs boson mass of 50 GeV. The black solid line indicates the exclusion boundary  $\mu = 1$ . Parameter combinations with larger values of  $\mu$  are excluded. Middle, expected exclusion limits at 90% CL on the spin-dependent DM-nucleon cross section as a function of  $m_{\text{DM}}$  for a dark Higgs boson mass hypothesis of 50 GeV. Right, expected exclusion limits at 90% CL on the spin-independent DM-nucleon cross section as a function of  $m_{\text{DM}}$  for a dark Higgs boson mass hypothesis of 50 GeV.

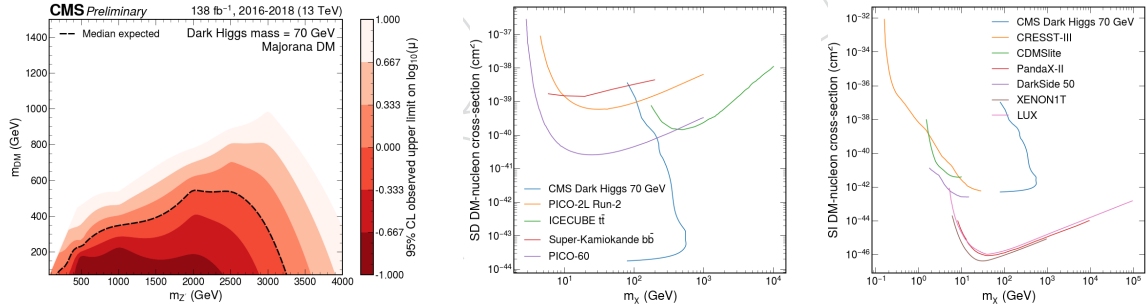


Figure 18: Left, expected exclusion limits at 95% CL on the signal strength  $\mu = \sigma/\sigma_{\text{theo}}$  as a function of  $m_{\text{med}}$  for a dark Higgs boson mass of 70 GeV. The black solid line indicates the exclusion boundary  $\mu = 1$ . Parameter combinations with larger values of  $\mu$  are excluded. Middle, expected exclusion limits at 90% CL on the spin-dependent DM-nucleon cross section as a function of  $m_{\text{DM}}$  for a dark Higgs boson mass hypothesis of 70 GeV. Right, expected exclusion limits at 90% CL on the spin-independent DM-nucleon cross section as a function of  $m_{\text{DM}}$  for a dark Higgs boson mass hypothesis of 70 GeV.

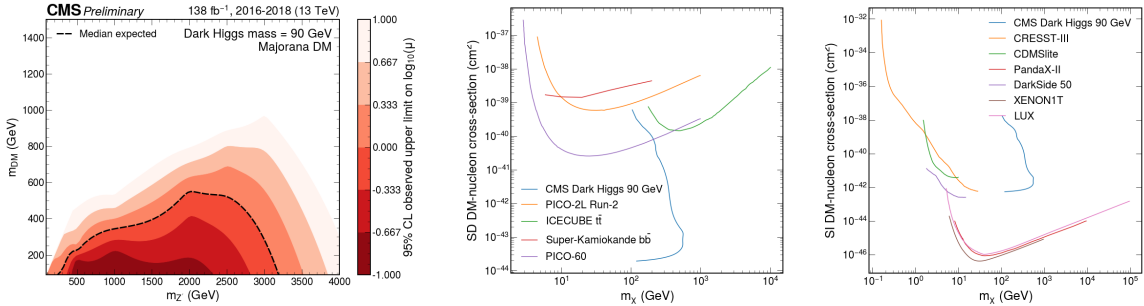


Figure 19: Left, expected exclusion limits at 95% CL on the signal strength  $\mu = \sigma/\sigma_{\text{theo}}$  as a function of  $m_{\text{med}}$  for a dark Higgs boson mass of 90 GeV. The black solid line indicates the exclusion boundary  $\mu = 1$ . Parameter combinations with larger values of  $\mu$  are excluded. Middle, expected exclusion limits at 90% CL on the spin-dependent DM-nucleon cross section as a function of  $m_{\text{DM}}$  for a dark Higgs boson mass hypothesis of 90 GeV. Right, expected exclusion limits at 90% CL on the spin-independent DM-nucleon cross section as a function of  $m_{\text{DM}}$  for a dark Higgs boson mass hypothesis of 90 GeV.

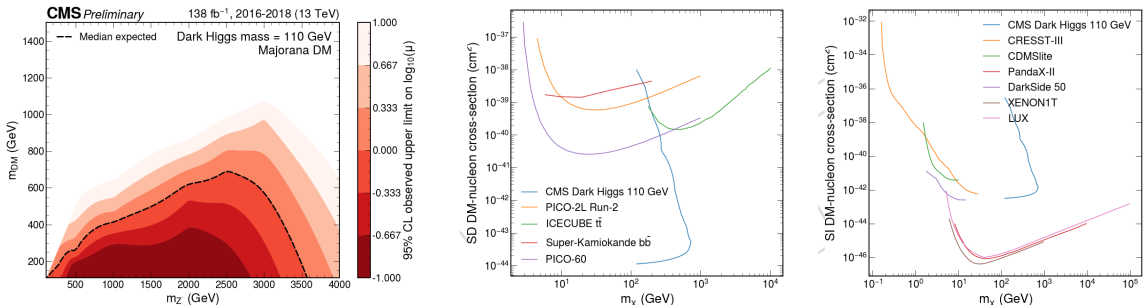


Figure 20: Left, expected exclusion limits at 95% CL on the signal strength  $\mu = \sigma/\sigma_{\text{theo}}$  as a function of  $m_{\text{med}}$  for a dark Higgs boson mass of 110 GeV. The black solid line indicates the exclusion boundary  $\mu = 1$ . Parameter combinations with larger values of  $\mu$  are excluded. Middle, expected exclusion limits at 90% CL on the spin-dependent DM-nucleon cross section as a function of  $m_{\text{DM}}$  for a dark Higgs boson mass hypothesis of 110 GeV. Right, expected exclusion limits at 90% CL on the spin-independent DM-nucleon cross section as a function of  $m_{\text{DM}}$  for a dark Higgs boson mass hypothesis of 110 GeV.

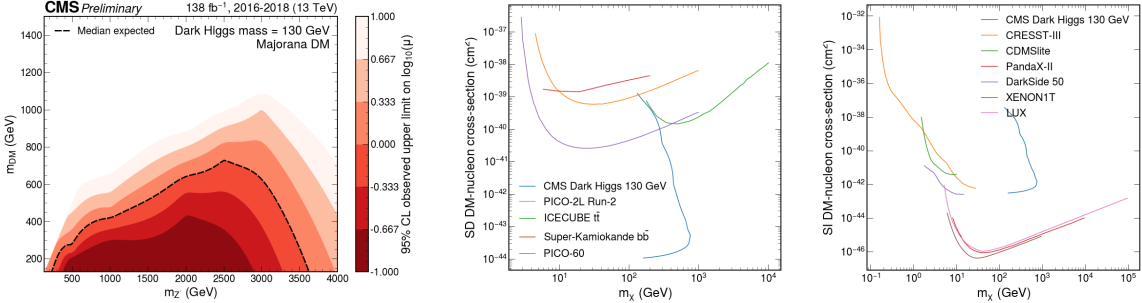


Figure 21: Left, expected exclusion limits at 95% CL on the signal strength  $\mu = \sigma/\sigma_{\text{theo}}$  as a function of  $m_{\text{med}}$  for a dark Higgs boson mass of 130 GeV. The black solid line indicates the exclusion boundary  $\mu = 1$ . Parameter combinations with larger values of  $\mu$  are excluded. Middle, expected exclusion limits at 90% CL on the spin-dependent DM-nucleon cross section as a function of  $m_{\text{DM}}$  for a dark Higgs boson mass hypothesis of 130 GeV. Right, expected exclusion limits at 90% CL on the spin-independent DM-nucleon cross section as a function of  $m_{\text{DM}}$  for a dark Higgs boson mass hypothesis of 130 GeV.

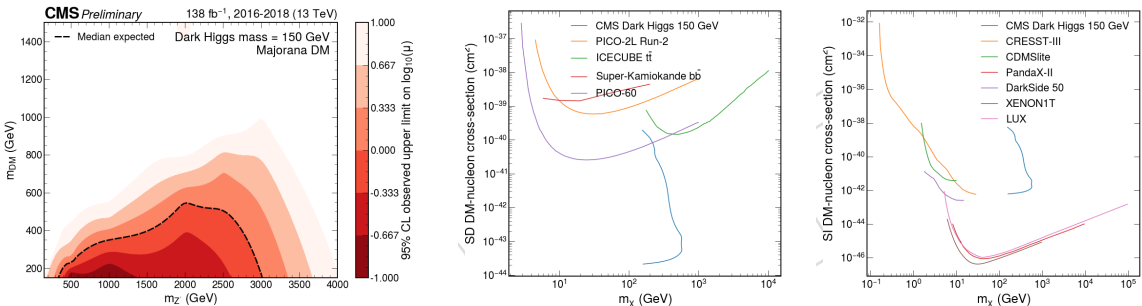


Figure 22: Left, expected exclusion limits at 95% CL on the signal strength  $\mu = \sigma/\sigma_{\text{theo}}$  as a function of  $m_{\text{med}}$  for a dark Higgs boson mass of 150 GeV. The black solid line indicates the exclusion boundary  $\mu = 1$ . Parameter combinations with larger values of  $\mu$  are excluded. Middle, expected exclusion limits at 90% CL on the spin-dependent DM-nucleon cross section as a function of  $m_{\text{DM}}$  for a dark Higgs boson mass hypothesis of 150 GeV. Right, expected exclusion limits at 90% CL on the spin-independent DM-nucleon cross section as a function of  $m_{\text{DM}}$  for a dark Higgs boson mass hypothesis of 150 GeV.

## 377 6 Summary

378 A search for physics beyond the standard model in events with a large-cone energetic jet consis-  
 379 tent with the hadronization of a resonant b-quark pair and large missing transverse momentum  
 380 has been presented. A data set of proton-proton collisions at a center-of-mass energy of 13 TeV,  
 381 corresponding to an integrated luminosity of 137.2 fb $^{-1}$  is analyzed. A joint maximum likeli-  
 382 hood fit over a combination of signal and control regions is used to constrain standard model  
 383 (SM) background processes and to extract a possible signal. The result is interpreted in terms  
 384 of exclusion limits at 95% confidence level on the parameters of a model of production of a  
 385 dark Higgs boson in association with dark matter particles. Values of the mediator mass of  
 386 up to 3–3.5 TeV are excluded, assuming the couplings of  $g_q = 0.25$  between the mediator and

387 quarks, and  $g_\chi = 1.0$  between the mediator and the DM particles. These constraints represent  
388 the most stringent bounds to date for dark Higgs boson masses below 160 GeV.

389 **Acknowledgments**

390 **References**

- [1] G. Bertone, D. Hooper, and J. Silk, “Particle dark matter: evidence, candidates and constraints”, *Phys. Rept.* **405** (2005) 279, doi:10.1016/j.physrep.2004.08.031, arXiv:hep-ph/0404175.
- [2] D. Abercrombie et al., “Dark matter benchmark models for early LHC Run-2 searches: report of the ATLAS/CMS dark matter forum”, 2015. arXiv:1507.00966.
- [3] CMS Collaboration, “Search for new particles in events with energetic jets and large missing transverse momentum in proton-proton collisions at  $\sqrt{s} = 13$  TeV”, *JHEP* **11** (2021) 153, doi:10.1007/JHEP11(2021)153, arXiv:2107.13021.
- [4] ATLAS Collaboration, “Search for new phenomena in events with an energetic jet and missing transverse momentum in  $pp$  collisions at  $\sqrt{s}=13$  TeV with the ATLAS detector”, *Phys. Rev. D* **103** (2021), no. 11, 112006, doi:10.1103/PhysRevD.103.112006, arXiv:2102.10874.
- [5] M. Duerr et al., “Hunting the dark higgs”, *Journal of High Energy Physics* **2017** (2017), no. 4, 143, doi:10.1007/JHEP04(2017)143.
- [6] ATLAS Collaboration, “Search for dark matter produced in association with a dark Higgs boson decaying into  $W^+W^-$  in the one-lepton final state at  $\sqrt{s}=13$  TeV using  $139\text{ fb}^{-1}$  of  $pp$  collisions recorded with the ATLAS detector”, *JHEP* **07** (2023) 116, doi:10.1007/JHEP07(2023)116, arXiv:2211.07175.
- [7] CMS Collaboration, “Search for dark matter particles in  $W^+W^-$  events with transverse momentum imbalance in proton-proton collisions at  $\sqrt{s} = 13$  TeV”, arXiv:2310.12229.
- [8] CMS Collaboration, “Performance of the CMS Level-1 trigger in proton-proton collisions at  $\sqrt{s} = 13$  TeV”, *JINST* **15** (2020) P10017, doi:10.1088/1748-0221/15/10/P10017, arXiv:2006.10165.
- [9] CMS Collaboration, “The CMS trigger system”, *JINST* **12** (2017) P01020, doi:10.1088/1748-0221/12/01/P01020, arXiv:1609.02366.
- [10] CMS Collaboration, “The CMS experiment at the CERN LHC”, *JINST* **3** (2008) S08004, doi:10.1088/1748-0221/3/08/S08004.
- [11] M. Cacciari, G. P. Salam, and G. Soyez, “The anti- $k_t$  jet clustering algorithm”, *JHEP* **04** (2008) 063, doi:10.1088/1126-6708/2008/04/063, arXiv:0802.1189.
- [12] M. Cacciari, G. P. Salam, and G. Soyez, “FastJet user manual”, *Eur. Phys. J. C* **72** (2012) 1896, doi:10.1140/epjc/s10052-012-1896-2, arXiv:1111.6097.
- [13] CMS Collaboration, “Particle-flow reconstruction and global event description with the CMS detector”, *JINST* **12** (2017) P10003, doi:10.1088/1748-0221/12/10/P10003, arXiv:1706.04965.

- [425] [14] CMS Collaboration, “Performance of missing transverse momentum reconstruction in  
426 proton-proton collisions at  $\sqrt{s} = 13$  TeV using the CMS detector”, *JINST* **14** (2019)  
427 P07004, doi:10.1088/1748-0221/14/07/P07004, arXiv:1903.06078.
- [428] [15] CMS Collaboration, “Jet energy scale and resolution in the CMS experiment in pp  
429 collisions at 8 TeV”, *JINST* **12** (2017) P02014,  
430 doi:10.1088/1748-0221/12/02/P02014, arXiv:1607.03663.
- [431] [16] CMS Collaboration, “Jet algorithms performance in 13 TeV data”, CMS Physics Analysis  
432 Summary CMS-PAS-JME-16-003, 2017.
- [433] [17] D. Bertolini, P. Harris, M. Low, and N. Tran, “Pileup per particle identification”, *JHEP* **10**  
434 (2014) 059, doi:10.1007/JHEP10(2014)059, arXiv:1407.6013.
- [435] [18] M. Dasgupta, A. Fregoso, S. Marzani, and G. P. Salam, “Towards an understanding of jet  
436 substructure”, *JHEP* **09** (2013) 029, doi:10.1007/JHEP09(2013)029,  
437 arXiv:1307.0007.
- [438] [19] J. M. Butterworth, A. R. Davison, M. Rubin, and G. P. Salam, “Jet substructure as a new  
439 Higgs search channel at the LHC”, *Phys. Rev. Lett.* **100** (2008) 242001,  
440 doi:10.1103/PhysRevLett.100.242001, arXiv:0802.2470.
- [441] [20] A. J. Larkoski, S. Marzani, G. Soyez, and J. Thaler, “Soft drop”, *JHEP* **05** (2014) 146,  
442 doi:10.1007/JHEP05(2014)146, arXiv:1402.2657.
- [443] [21] T. Sjöstrand et al., “An introduction to PYTHIA 8.2”, *Comput. Phys. Commun.* **191** (2015)  
444 159, doi:10.1016/j.cpc.2015.01.024, arXiv:1410.3012.
- [445] [22] CMS Collaboration, “Extraction and validation of a new set of CMS PYTHIA8 tunes from  
446 underlying-event measurements”, arXiv:1903.12179.
- [447] [23] GEANT4 Collaboration, “GEANT4—a simulation toolkit”, *Nucl. Instrum. Meth. A* **506**  
448 (2003) 250, doi:10.1016/S0168-9002(03)01368-8.
- [449] [24] The NNPDF collaboration et al., “Parton distributions for the lhc run ii”, *Journal of High  
450 Energy Physics* **2015** (2015), no. 4, 40, doi:10.1007/JHEP04(2015)040.
- [451] [25] NNPDF Collaboration, “Parton distributions from high-precision collider data”, *Eur.  
452 Phys. J.* **C77** (2017), no. 10, 663, doi:10.1140/epjc/s10052-017-5199-5,  
453 arXiv:1706.00428.
- [454] [26] J. Alwall et al., “The automated computation of tree-level and next-to-leading order  
455 differential cross sections, and their matching to parton shower simulations”, *JHEP* **07**  
456 (2014) 079, doi:10.1007/JHEP07(2014)079, arXiv:1405.0301.
- [457] [27] M. L. Mangano, M. Moretti, F. Piccinini, and M. Treccani, “Matching matrix elements and  
458 shower evolution for top-quark production in hadronic collisions”, *JHEP* **01** (2007) 013,  
459 doi:10.1088/1126-6708/2007/01/013, arXiv:hep-ph/0611129.
- [460] [28] R. Frederix and S. Frixione, “Merging meets matching in MC@NLO”, *JHEP* **12** (2012)  
461 061, doi:10.1007/JHEP12(2012)061, arXiv:1209.6215.
- [462] [29] M. Czakon, P. Fiedler, and A. Mitov, “Total top-quark pair-production cross section at  
463 hadron colliders through  $o(\alpha_s^4)$ ”, *Phys. Rev. Lett.* **110** (2013) 252004,  
464 doi:10.1103/PhysRevLett.110.252004, arXiv:1303.6254.

- [30] S. Alioli, P. Nason, C. Oleari, and E. Re, “NLO single-top production matched with shower in POWHEG:  $s$ - and  $t$ -channel contributions”, *JHEP* **09** (2009) 111, doi:10.1088/1126-6708/2009/09/111, arXiv:0907.4076. [Erratum: doi:10.1007/JHEP02(2010)011].
- [31] E. Re, “Single-top Wt-channel production matched with parton showers using the POWHEG method”, *Eur. Phys. J. C* **71** (2011) 1547, doi:10.1140/epjc/s10052-011-1547-z, arXiv:1009.2450.
- [32] M. Aliev et al., “HATHOR: HAdronic Top and Heavy quarks crOss section calculatoR”, *Comput. Phys. Commun.* **182** (2011) 1034, doi:10.1016/j.cpc.2010.12.040, arXiv:1007.1327.
- [33] P. Kant et al., “HATHOR for single top-quark production: Updated predictions and uncertainty estimates for single top-quark production in hadronic collisions”, *Comput. Phys. Commun.* **191** (2015) 74, doi:10.1016/j.cpc.2015.02.001, arXiv:1406.4403.
- [34] T. Gehrmann et al., “ $W^+W^-$  production at hadron colliders in next to next to leading order QCD”, *Phys. Rev. Lett.* **113** (2014) 212001, doi:10.1103/PhysRevLett.113.212001, arXiv:1408.5243.
- [35] J. M. Campbell and R. K. Ellis, “An update on vector boson pair production at hadron colliders”, *Phys. Rev. D* **60** (1999) 113006, doi:10.1103/PhysRevD.60.113006, arXiv:hep-ph/9905386.
- [36] LHC Dark Matter Working Group, “Recommendations of the LHC dark matter working group: Comparing LHC searches for dark matter mediators in visible and invisible decay channels and calculations of the thermal relic density”, *Phys. Dark Univ.* **26** (2019) 100377, doi:10.1016/j.dark.2019.100377, arXiv:1703.05703.
- [37] CMS Collaboration, “Identification of heavy, energetic, hadronically decaying particles using machine-learning techniques”, *JINST* **15** (2020), no. 06, P06005, doi:10.1088/1748-0221/15/06/P06005, arXiv:2004.08262.
- [38] CMS Collaboration, “Electron and photon reconstruction and identification with the CMS experiment at the CERN LHC”, *JINST* **16** (2021) P05014, doi:10.1088/1748-0221/16/05/P05014, arXiv:2012.06888.
- [39] CMS Collaboration, “Performance of the CMS muon detector and muon reconstruction with proton-proton collisions at  $\sqrt{s} = 13$  TeV”, *JINST* **13** (2018) P06015, doi:10.1088/1748-0221/13/06/P06015, arXiv:1804.04528.
- [40] C. Collaboration, “Identification of hadronic tau lepton decays using a deep neural network”, *JINST* **17** (2022) P07023, doi:10.1088/1748-0221/17/07/P07023, arXiv:2201.08458.
- [41] E. Bols et al., “Jet Flavour Classification Using DeepJet”, *JINST* **15** (2020), no. 12, P12012, doi:10.1088/1748-0221/15/12/P12012, arXiv:2008.10519.
- [42] J. M. Lindert et al., “Precise predictions for V+jets dark matter backgrounds”, *Eur. Phys. J. C* **77** (2017) 829, doi:10.1140/epjc/s10052-017-5389-1, arXiv:1705.04664.

- 505 [43] CMS Collaboration, “Performance of the CMS missing transverse momentum  
506 reconstruction in pp data at  $\sqrt{s} = 8$  TeV”, *JINST* **10** (2015) P02006,  
507 doi:10.1088/1748-0221/10/02/P02006, arXiv:1411.0511.
- 508 [44] CMS Collaboration, “Search for new physics in final states with an energetic jet or a  
509 hadronically decaying W or Z boson and transverse momentum imbalance at  
510  $\sqrt{s} = 13$  TeV”, *Phys. Rev. D* **97** (2018) 092005, doi:10.1103/PhysRevD.97.092005,  
511 arXiv:1712.02345.
- 512 [45] J. Conway, “Incorporating Nuisance Parameters in Likelihoods for Multisource Spectra”,  
513 doi:10.5170/CERN-2011-006.115, arXiv:1103.0354. Comments: Presented at  
514 PHYSTAT 2011, CERN, Geneva, Switzerland, January 2011, to be published in a CERN  
515 Yellow Report.
- 516 [46] A. L. Read, “Presentation of search results: The  $CL_s$  technique”, *J. Phys. G* **28** (2002) 2693,  
517 doi:10.1088/0954-3899/28/10/313.
- 518 [47] T. Junk, “Confidence level computation for combining searches with small statistics”,  
519 *Nucl. Instrum. Meth. A* **434** (1999) 435, doi:10.1016/S0168-9002(99)00498-2,  
520 arXiv:hep-ex/9902006.
- 521 [48] G. Cowan, K. Cranmer, E. Gross, and O. Vitells, “Asymptotic formulae for  
522 likelihood-based tests of new physics”, *Eur. Phys. J. C* **71** (2011) 1554,  
523 doi:10.1140/epjc/s10052-011-1554-0, arXiv:1007.1727. [Erratum:  
524 doi:10.1140/epjc/s10052-013-2501-z].
- 525 [49] G. Busoni et al., “Recommendations on presenting LHC searches for missing transverse  
526 energy signals using simplified s-channel models of dark matter”, *Phys. Dark Univ.* **27**  
527 (2020) 100365, doi:10.1016/j.dark.2019.100365, arXiv:1603.04156.